3D Nanocomposites of Covalently Interconnected Multiwalled Carbon Nanotubes with SiC with Enhanced Thermal and Electrical Properties

*Lakshmy Pulickal Rajukumar, Manuel Belmonte, John Edward Slimak, Ana Laura Elías, Eduardo Cruz-Silva, Nestor Perea-López, Aaron Morelos-Gómez, Humberto Terrones, Morinobu Endo, Pilar Miranzo, and Mauricio Terrones**

Synthesizing 3D carbon nanotube (CNT) networks with multifunctional characteristics has stimulated the interest from the scientific community since the 1990s. Here, the fabrication of a novel composite material consisting of 3D covalently interconnected multiwalled CNT with silicon carbide (SiC) nano and microparticles is reported. The material is synthesized by a two-step process involving the coating of CNT with silicon oxide (SiO_x) via chemical routes, followed by spark plasma sintering (SPS). SPS enables carbothermal reduction of SiO_x and subsequent densification of the material into 3D composite blocks. Covalent interconnections of CNT are facilitated by a carbon diffusion process resulting in SiC formation as SiO_x coated CNT are subjected to high temperatures. The presence of SiC in the sintered composite has been confirmed by Raman spectroscopy, as well as through energy filtered transmission electron microscopy maps. Interestingly, the 3D CNT composite exhibits high thermal conductivity (16.72 W m^{-1} K^{-1}); and also a semiconducting behavior with an electron hopping mechanism associated to a 3D variable range hopping model. These findings demonstrate that it is indeed possible to fabricate SiC–CNT composites with enhanced physical properties that can be used as multifunctional materials.

1. Introduction

Carbon nanotubes (CNT) are unique 1D nanostructures composed of sp^2 hybridized carbon atoms. Their remarkable electronic and mechanical properties have been intriguing for more than two decades.[1] The presence of strong carbon–carbon bonds is one of the reasons why nanostructures made from sp^2 carbon generally exhibit outstanding mechanical properties. For instance, CNT are very stiff, strong, and mechanically robust nanomaterials whose stiffness can reach values of up to 1 TPa.[2] When using these nanostructures as building blocks for macrostructures, it is possible to achieve unusual mechanical and electronic properties.[3] Besides these properties, the very high specific surface area (of the order of ≈2000 m^2 g^{-1})[4] in these materials makes them promising candidates for gas adsorption, catalysis, filtration, and sensing applications.[3–7]

L. Pulickal Rajukumar
Department of Materials Science and Engineering
The Pennsylvania State University
University Park, PA 16802, USA

Dr. M. Belmonte, Prof. P. Miranzo
Institute of Ceramics and Glass (ICV-CSIC)
Campus de Cantoblanco
Kelsen 5, 28049 Madrid, Spain

J. E. Slimak
Department of Chemical Engineering
The Pennsylvania State University
University Park, PA 16802, USA

Dr. A. L. Elías, Dr. E. Cruz-Silva, Dr. N. Perea-López, Prof. M. Terrones
Department of Physics and Center for 2-Dimensional and Layered Materials
The Pennsylvania State University
University Park, PA 16802, USA
E-mail: mut11@psu.edu

Dr. A. Morelos-Gómez, Prof. M. Endo, Prof. M. Terrones
Carbon Institute of Science and Technology
Shinshu University
Wakasato 4-17-1, Nagano-city 380-8553, Japan

Prof. H. Terrones
Department of Physics
Applied Physics and Astronomy
Rensselaer Polytechnic Institute
Troy, NY 12180, USA

Prof. M. Terrones
Department of Materials Science and Engineering
The Pennsylvania State University
University Park, PA 16802, USA

DOI: 10.1002/adfm.201501696

In this regard, there has been interest for developing novel 3D carbon nanotube-based structures that are multifunctional. Some approaches for developing these new materials involve synthetic techniques such as chemical vapor deposition (CVD),[8,9] while others involve postprocessing routes, such as forming CNT aerogels or chemical crosslinking.[10,11]

However, there is still a necessity to explore novel and scalable methods in order to overcome the challenge of establishing covalent interconnections between carbon nanotubes. Spark plasma sintering (SPS) is a relatively new technique used for densifying a large variety of ceramics, composites, and metals.[12] In essence, SPS is a pressure-assisted furnace in which the heating is provided by a pulsed direct current supplied to the graphite die containing the powders to be sintered. In addition, current-assisted heating allows rapid heating rates up to high temperatures. SPS has recently been used for fabricating a variety of nanocarbon (particularly graphene and CNT) reinforced metal and ceramic matrix composites.[13–15] These materials are sought after for various industrial applications, particularly in automobile and aerospace industries. In recent studies, SPS was successfully used to fabricate homogeneously dispersed dense silicon carbide (SiC)/graphene nanoplatelets (GNPs) composites by liquid-phase sintering of SiC–GNPs powder mixtures with GNPs contents up to 20 vol.%,[16] and to manufacture SiC/graphene composites by in situ synthesizing graphene sheets at SiC grain boundaries during the SPS densification of SiC ceramics.[17] This and other studies reveal how SPS is a novel cost-effective technique to produce composites.

We propose here the use of SPS for the fabrication of a composite material comprising 3D interconnected CNT as the framework. The covalent interconnection of the CNT network has been facilitated by a carbon diffusion process resulting in SiC formation as silica (SiO_2)-coated CNT are subjected to high temperatures (**Figure 1**). The temperature that was found to be most effective for carbothermal reduction of silica to SiC is 1800 °C. The use of SPS for the fabrication of the novel SiC–CNT composites reported here has allowed the reaching of high temperatures and pressures required for the carbothermal reduction of silica, as well as to densifying the material into a stable 3D composite block.

2. Results and Discussion

Various theories have been proposed for the carbothermal reduction of SiO_2 to form SiC. The general consensus is that at temperatures above 1400 °C silica melts, and when carbon is present, SiC can nucleate from a reaction between Si and C according to Equation (1)[18,19]

$$SiO_2(s,l) + 3C(s) \rightarrow SiC(s) + 2CO(g) \quad (1)$$

The amount of synthesized SiC depends on the activity of carbon and the partial pressure of CO gas that is a byproduct of the reaction between SiO_2 and C. The ease with which CO gas escapes from the pores during sintering is believed to enhance the densification of the material and also the SiC formation.[20] Early studies on carbothermal reduction process of SiO_2 mention a link between the final particle sizes of SiC crystallites and the size of carbon clusters (precursors), time of reaction as well as reaction temperature.[21,22] In general, for sintering processes the final grain structures are highly dependent on the sintering temperature and time. Krstic et al. also mention the dependence of SiC crystallite size to the size of SiO_2 clusters to produce high-purity SiC using carbothermal reduction process. Their findings indicate that the reaction rate (for the conversion of SiO_2 to SiC) governs the SiC domain formation and it is dependent on SiO_2 cluster size. For small SiO_2 particles in contact with carbon, these authors observe an enhanced rate of solid-state reaction between carbon and SiO_2. In addition, once the solid-state reaction starts, the gas formed (CO) has to be continuously removed from the system for the reaction to proceed. Furthermore, the diffusion of Si and C through the SiC further limits the reaction. But since CNTs have very high surface area, we are able to overcome some of these limitations that would otherwise suppress the reaction. Scanning electron microscopy (SEM) images (**Figure 2**c,d) of the sintered sample show fractured surfaces of the SiC–CNT composite. We clearly observe a dense composite material with a high CNT loading in comparison with other SiC–CNT composites previously reported in the literature.[23,24] The high densification is expected to be a direct result of using high pressure in addition to high temperature during sintering. Interestingly, we also observed that the extremely high uniaxial pressure can give rise to partial 2D alignment of CNTs perpendicular to the direction of the applied pressure (see Figure S2, Supporting Information). Although some CNT appear slightly damaged, there seems to be a good adherence between the CNT in general. The length of the tubes ranges from a few hundred nanometers to a few micrometers and the diameters vary from 20 to 70 nm.

The average Raman spectrum of the sample SPSed at 1800 °C (**Figure 3**a) revealed the coexistence of graphitic species (D-, G-, and 2D-bands for sp^2 hybridized carbon) and SiC (≈800 and 972 cm^{-1}). From this spectrum, it was possible to identify the spatial distribution of each component on the scanned map as well as their characteristic spectra. A Raman image in false colors was created using these data (Figure 3b), mapping the intensity of the G-band (in blue) and the SiC band at 800 cm^{-1} (in red). Two representative spectra at different positions of the Raman image (marked as 1 and 2 in Figure 3b) were extracted and are shown in Figure 3a. In this context, the spectrum at position 1 (blue) corresponds to crystalline CNT, which was confirmed by the low intensity ratio between the D- and G-bands ($I_D/I_G = 0.45$) obtained even after the extreme SPS conditions. The spectrum at position 2 (red) confirmed the formation of SiC, depicting two clear peaks ascribed to transverse-optical (≈800 cm^{-1}) and longitudinal-optical (≈972 cm^{-1}) modes of β-SiC. In addition, the Raman image also shows the homogenous distribution of SiC within the CNT network.

In order to further probe the crystalline structure of the composite, X-ray diffraction (XRD) was employed. The XRD pattern of the SiC-CNT composite after the sintering process is shown in Figure 3c. Peak fitting analysis of the diffractogram revealed the prominent peaks belonging to CNT and β-SiC.[25,26] The presence of SiC is clearly indicated by the peaks located at 2θ values 36°, 42°, 61°, and 72°, corresponding to SiC(111), (200), (220), and (311) interplanar spacing. A splitting of the C(002) peak is observed and this can be attributed to the formation of small graphitic domains during the carbon diffusion process.

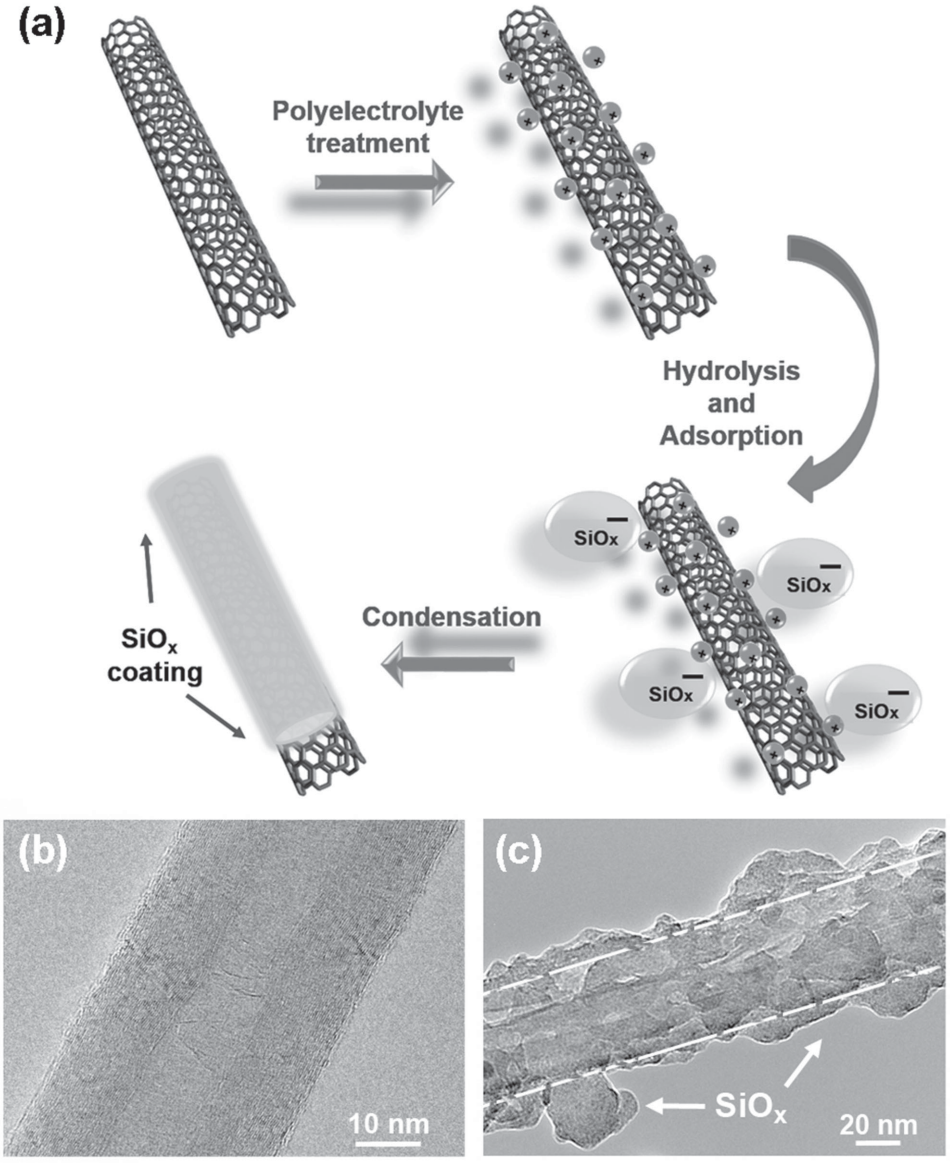

Figure 1. a) Schematic of the sol–gel process, b) TEM image of a multiwalled CNT before the sol–gel process, and c) SiO*x*-coated MWNT after the sol–gel process.

These domains are expected to be turbostratic in nature with an offset in their d-spacing.

From both Raman spectroscopy and XRD techniques, a fairly good degree of crystallinity within CNT can be observed after the SPS process. While correlating this with SEM images of the composite it can be observed that the crystalline structure of most CNT was retained, even after subjecting them to high temperature and extreme pressure. The I_D/I_G value of 0.45 observed in the Raman spectrum of SiC–CNT composite reveal lesser amount of damage to the tubes as compared to other studies that report a higher I_D/I_G ratio of CNTs after SPS process.[27] While our starting CNT material had an I_D/I_G of 0.35 (see Figure S3, Supporting Information), we believe that the sintering conditions we have used (1800 °C, 80 MPa of pressure for 10 min, instead of 1300 °C, 60 MPa pressure for 5 min which is reported in ref. [27] have not resulted in much damage to the tubes and improve the crystallinity of the overall sample. Newly formed SiC domains of different sizes (ranging from 5 to 10 μm) are observed throughout the composite, bundling as well as interconnecting the CNT. Those bundles are expected to be composed of junctions of CNT and SiC, which is further confirmed using high-resolution transmission electron microscopy (HRTEM).

HRTEM images (**Figure 4**) of the composite show CNT in a mixed amorphous and crystalline matrix. Fast Fourier transformation (FFT) of the lattice fringes as well as the interplanar spacing helped to identify CNT and SiC within the sample. From low magnification images it can be observed that the SiC nucleation occurs very close to the CNT walls. Smaller domains of SiC are first formed when carbon atoms from the CNT walls react with SiO_x that surrounds them. At this point, SiC domains

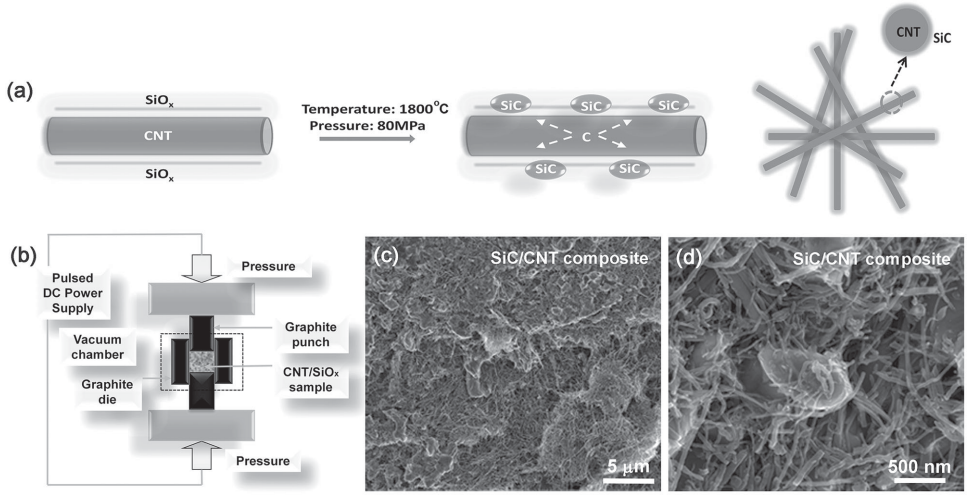

Figure 2. a) Schematic diagram representing the carbothermal reduction of silica and 3D CNT network formation during SPS, b) schematic view of the SPS experimental setup, and c,d) SEM images of SiC–CNT composite.

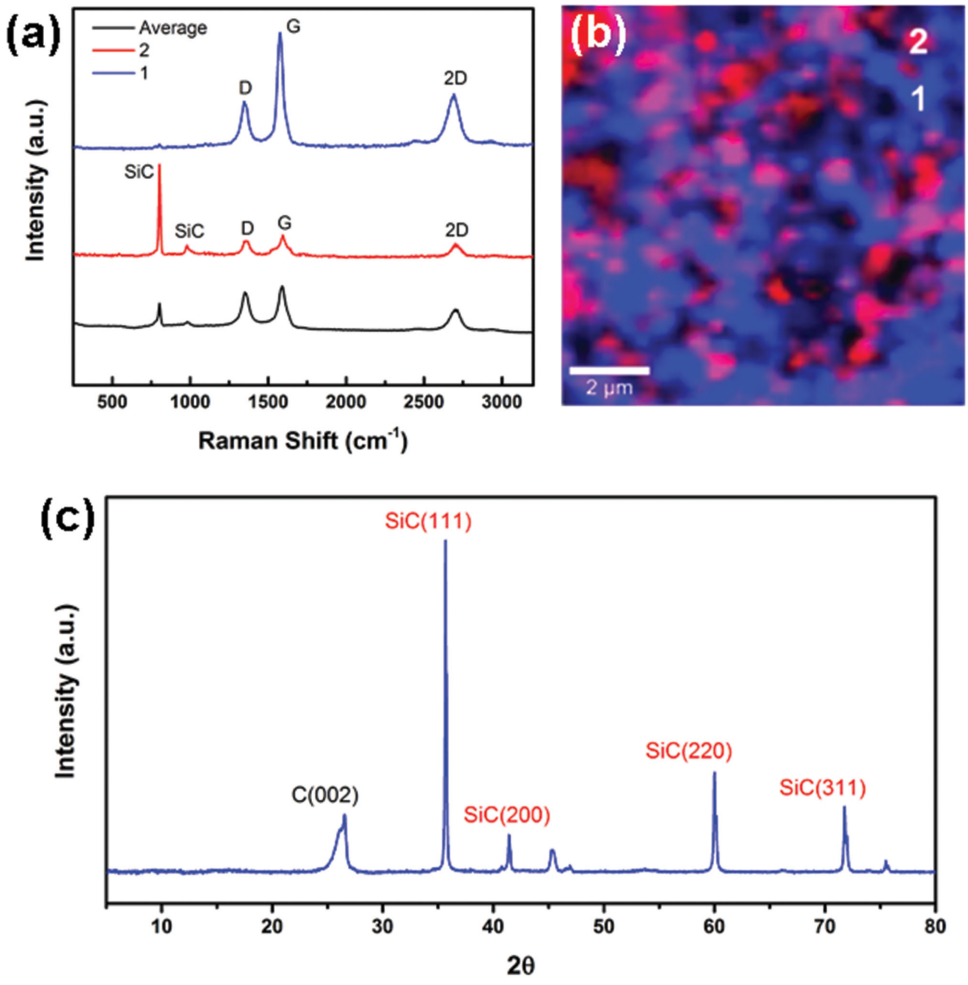

Figure 3. a) Raman spectra of spark plasma sintered SiC–CNT composite showing an average Raman spectrum and individual SiC and CNT spectra from regions 1 and 2 in Figure 3b; b) Raman image (in false colors) on a scanned area of 10 μm × 10 μm created by mapping the intensity of the G-band of CNT (blue) and the 800 cm^{-1} band of SiC (red), and c) XRD pattern of SiC–CNT composite showing the graphitic C(002) reflection and the presence of the β-SiC phase in the composite.

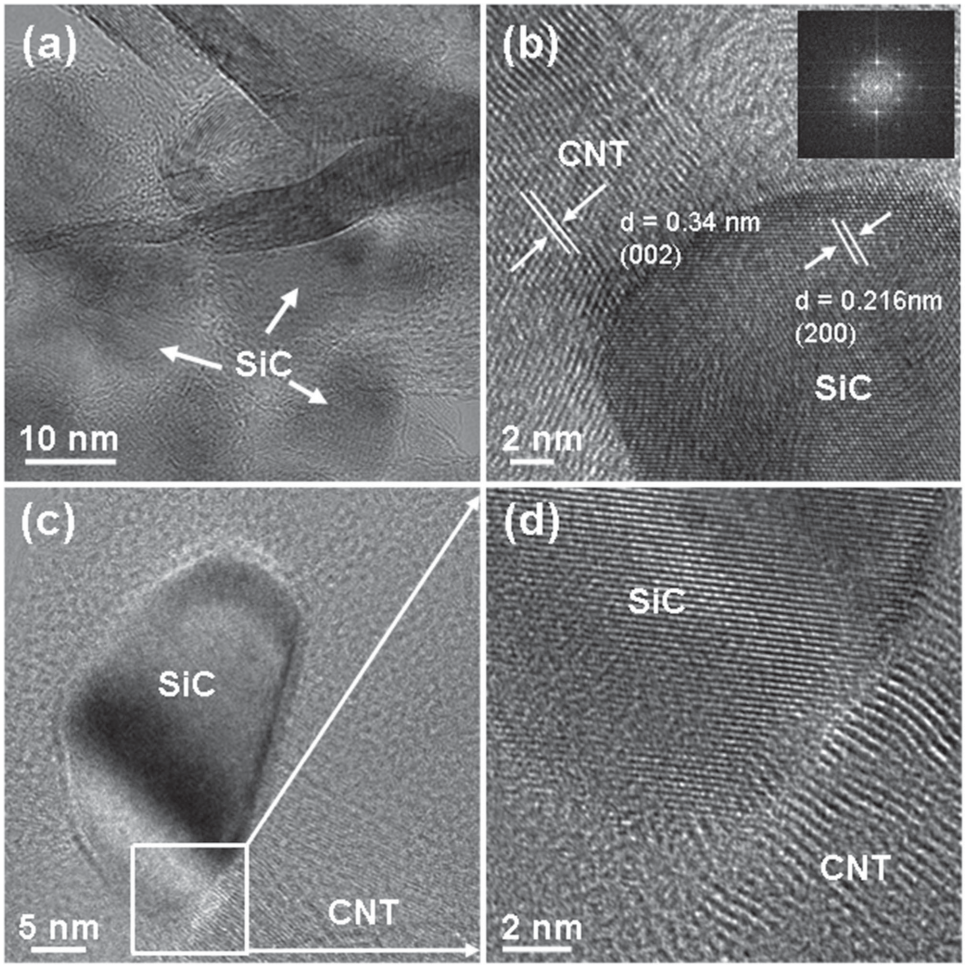

Figure 4. a–d) HRTEM images of SiC-CNT composite showing SiC domains around the graphitic planes of MWNTs. Inset in (b) shows the FFT of SiC region.

sometimes merge to form larger crystallites that are of the order of ≈10 µm in size. On a closer look at the high-resolution images of the composite, lattice fringes of SiC deriving from the CNT walls (Figure 4b–d) are clearly identified. This further confirms the occurrence of carbothermal conversion of silica into SiC.

Energy dispersive X-ray spectroscopy (EDS) was used to obtain microscopic elemental information of the synthesized samples. An EDS spectrum shows characteristic peaks for C, Si, and Fe as shown in **Figure 5**a. Energy filtered transmission electron microscopy (EFTEM) imaging has been previously used for analyzing the 3D nature of composites containing CNT, especially in cases where the CNT are embedded in an amorphous matrix.[28] In the EFTEM maps obtained from the SiC–CNT composite, CNT are embedded in a matrix containing carbon and silicon. The zero loss map in Figure 5b can be compared to a regular bright field HRTEM image of the specimen, in which the bright portion corresponds to vacuum and the dark portions correspond to thick regions of the sample. Figure 5c shows an elemental map in which the brighter areas correspond to the region with carbon. As expected, the carbon signal is observed throughout the sample, from CNT as well as SiC; and the presence of CNT within the matrix is revealed by the brighter elongated areas within the SiC particles. The distribution of CNT in the matrix is more evident in the corresponding silicon map (Figure 5d), in which a good correlation with the carbon map is observed, with the exception of dark elongated areas that correspond to the location of the CNT identified in Figure 5c.

Thermal conductivity (k), diffusivity (α), and density measurements (ρ) were carried out on the sintered sample. Since the specimens exhibited a high surface roughness, the maximum surface roughness (R_{max} = 39 µm) was used to correct the experimental α data. According to previous studies by some of the present authors, the value of actual thickness was obtained by subtracting twice the value of R_{max} from the measured thickness.[29,30] The obtained values are listed in **Table 1**. "k" values of the sintered block before and after the correction are 16.72 and 14.15 W m^{-1} K^{-1}, respectively. The results were compared to those previously reported for similar nanocarbon-based materials, such as CNT buckypaper and bulk specimens of pressed GNPs.[31] Analysis of the thermal properties of the SiC–CNT composite in a through-thickness direction shows thermal conductivity values about two orders of magnitude higher than those observed for buckypaper. This is expected because buckypaper has a lower density. It was previously found that adding small weight fractions of CNT to a thermally conducting matrix can increase anisotropy in

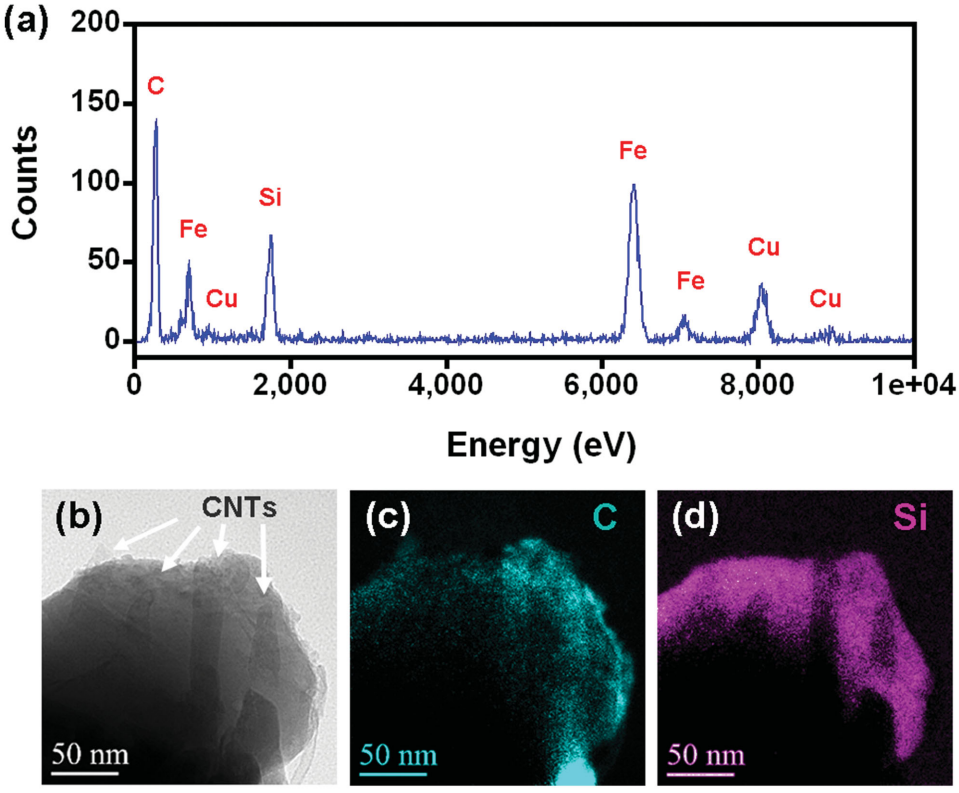

Figure 5. a) Presence of silicon and carbon was further confirmed using EDS in a HRTEM and b–d) EFTEM elemental maps of zero loss, carbon and silicon map (respectively), clearly showing CNTs embedded in a SiC matrix.

the thermal conduction behavior of the resultant composite.[31] A strong correlation between the amount of CNT and the reduction in the through-thickness value of k (in the uniaxial pressing direction) has also been found. This has been attributed to the presence of thermal interfaces between CNT and the matrix material, as well as to intertube interactions. There are reports of CNT blocks sintered using SPS without the addition of any matrix material having thermal conductivity values in the range of 12 W m^{-1} K^{-1}.[32] In this case, a percolation network of CNT is believed to create a 3D phonon conduction mechanism when high sintering temperatures (>1500 °C) are employed. In the present work, the creation of intertube and SiC–CNT junctions has a combinatorial effect on the thermal properties.

From the electrical measurements, it is observed that the resistivity rapidly decreases with increasing temperature in the regime 2–10 K, and on further increasing the temperature, the resistivity decreases more gradually. This is a typical response observed for semiconducting materials. A comparative study was also performed by measuring the resistivity of the SiC–CNT sample sintered at 1800 °C and of a sample sintered at 1700 °C, keeping the rest of the experimental conditions constant. The resistivity of the SiC–CNT composite sintered at 1800 °C was found to be 4.77×10^{-2} and of 5.19×10^{-3} Ω cm for the sample sintered at 1700 °C. This is significantly lower than that of pure SiC, as reported in the literature.[33]

Table 2 shows a comparison of the electrical resistivity of different SiC-based materials.[17,23,34–37] We have also compared

Table 1. Density (ρ), thermal diffusivity (α), and thermal conductivity (k) of the SPSed SiC–CNT material. A comparison with other graphitic materials measured at 27 °C in the through-thickness direction has also been included.

Material	ρ [g cm^{-3}]	α [cm^2 s^{-1}]	k [W m^{-1} K^{-1}]
Buckypaper [29]	0.51	0.0056	0.20
GNPs[29]	1.80	0.0283	3.62
SiC–CNT (this work)	1.74	0.1354	16.72
SiC–CNT[a)] (this work)	1.74	0.1146	14.15

[a)]Data corrected using R_{max}.

Table 2. Resistivity (Ω cm, @ 300 K) of the SPSed SiC–CNT material in comparison with other SiC and CNT-based materials.

Material	Resistivity [Ω cm, @ 300 K]
CNT-reinforced SiC [21]	0.334–0.065
Nano β-SiC [17]	0.99
α-SiC[17]	1.25×10^6
SiC[32,33]	1×10^8–1×10^{20}
MWNT blocks[34]	2×10^{-3}–3×10^{-3}
Cross-linked CNT (CL-CNT) blocks[35]	4.16×10^{-2}
SiC–CNT (this work)	4.72×10^{-2}

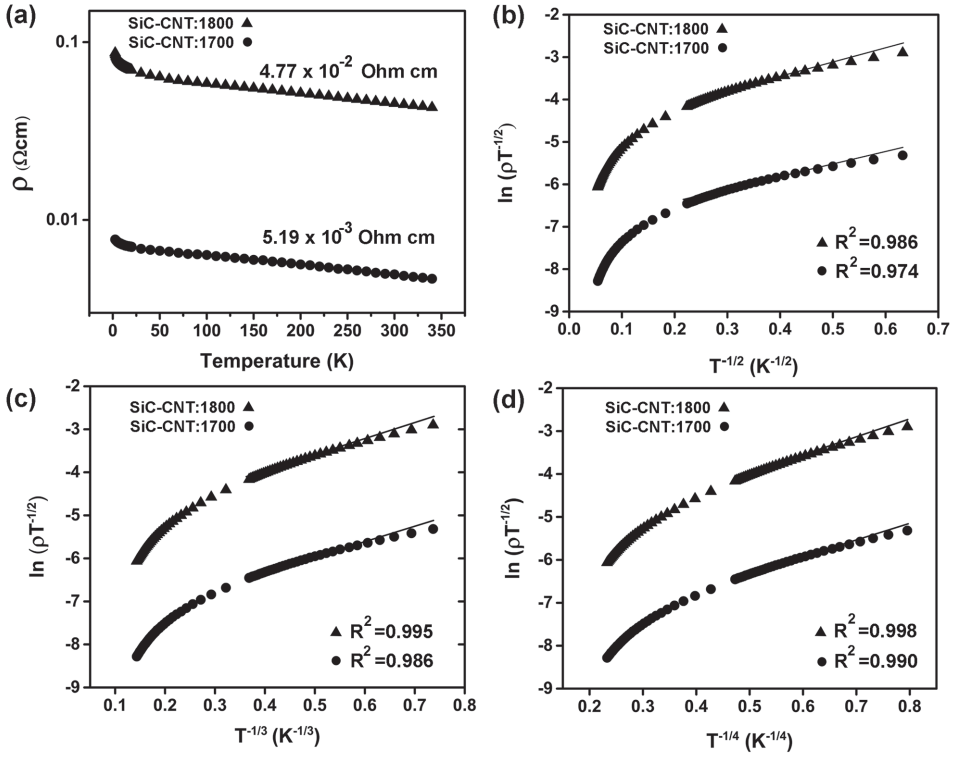

Figure 6. a) Electrical resistivity as a function of temperature measured for SiC–CNT samples sintered at 1700 and 1800 °C. At 1800 °C, we believe that a more efficient reduction of SiO_2 to SiC takes place that results in lower electrical conductivity values. b–d) Variable range hopping models for SiC–CNT composites. The 3D VRH model shows the highest regression value.

the electrical resistivity to pure CNT samples in order to determine where our sample fits in. The addition of CNT to SiC has been previously found to improve the electrical conductivity of SiC by 96%.[23] The SiC-CNT composite that we have fabricated has an optimum value of electrical conductivity, integrating the properties of electrically insulating SiC and conductive CNT.[32,33,38] From the TGA curve of the SiC–CNT sample (see the Supporting Information for more details), we witness a weight loss of ≈30% close to 600 °C. This is an indicative of the amount of residual graphitic carbon content in the sample after the sintering process. Having formed a large fraction of SiC during the sintering process, we would expect the composite to be more insulating as compared to a block of sintered CNT without any SiC. On the contrary, the electrical conductivity of our composite is comparable to other CNT-based materials thereby suggesting that the high electrical conductivity of the SiC–CNT is a direct consequence of interlinking of CNT during the SPS process. The resistivity value measured for the sample sintered at 1800 °C is one order of magnitude higher than that of the sample sintered at 1700 °C. The probable reason for this behavior is the elevation in the carbothermal reduction rate with increasing the sintering temperature.

We have also used variable range hopping (VRH) models to predict the electron hopping mechanism in these composites, as shown in **Figure 6**. VRH was proposed by Mott in 1969.[39] These models were obtained by plotting $\ln(\rho T^{-1/2})$ as a function of $T^{-1/(n+1)}$, where $n = 1$, 2, or 3 indicate the dimensionality of the sample. Figure 6b–d shows VRH models for $n = 1$, 2, and 3, respectively. Fitting the linear region of the above-mentioned plot gives an insight into the conduction mechanism which prevails in the sample. The best fit corresponds to the one with the highest correlation coefficient (R^2). For the SiC–CNT composite, the value of the regression coefficient was found to be highest for the linear portion in the 3D VRH model fitting, indicating that the electron hopping mechanism in the SiC–CNT composite occurs in three dimensions. From previously reported studies regarding electron conduction mechanisms in CNT composites, 1D VRH is the most prominent form of charge transport.[40] This arises from the expected charge tunneling property of CNT. Nevertheless, the carbothermal reduction process for the SiC–CNT samples results in the creation of an interconnected CNT network through carbon diffusion. Charge transport is facilitated in the bulk sample through these 3D charge pathways as a result of the crystallization of SiC from SiO_x-CNT.

3. Conclusions

We report here a novel approach to fabricate CNT-based 3D composite materials using a postprocessing technique that involves the coating of CNTs with SiO_x followed by SPS (at high temperature). SiO_x undergoes a carbothermal reduction during the sintering process at 1800 °C to form SiC by a carbon diffusion process between the CNT and SiO_x. The newly formed SiC matrix interconnects the CNT in the SiC–CNT composite.

SPS has shown excellent potential for creating numerous CNT interconnections for the fabrication of 3D bulk structures. The presence of SiC in the sintered composite has been confirmed through spectroscopic studies and microstructural analysis. Thermal and electrical properties of the sintered composite are outstanding and constitute an indicator of the formation of covalent interconnections between the tubes. It has already been established that the addition of CNT can considerably lower the electrical resistivity of ceramic materials.[23] By incorporating CNT in a SiC matrix, we have not only improved the electrical conductivity values but also preserved the excellent thermal conductivity of the material. This could potentially serve as a good ceramic/CNT composite for electromagnetic shielding for aeronautic applications.

4. Experimental Section

The CNT (pristine multiwalled carbon nanotubes) used in this study were synthesized using an aerosol-assisted CVD with toluene as the carbon source and iron as the catalyst. Details of this process are reported in ref.[41]. The as-synthesized tubes were subjected to a peroxide treatment (ultrasonication in hydrogen peroxide at 1 mg mL^{-1} concentration for 8 h), in order to segregate the tube bundles to improve their dispersion in the subsequent sol–gel process.

The SiC–CNT composite material was fabricated by a two-step process as illustrated in Figure 1. The first step involved coating the CNT with SiO_x by a sol–gel process, as described by Seeger et al.[42] The process involves ultrasonication of peroxide treated CNT (1 g) in polyethylemine (PEI, 0.25 wt.% solution). PEI helps creating positive charges on the surface of CNT. After removing excess PEI by ultracentrifugation at 5000 rpm for 1–2 h, the residue was rinsed thoroughly with water. This was followed by adsorption of negatively charged SiO_x colloidal particles on the external walls of CNT. For this, a sol was prepared by hydrolysis and ondensation of tetraethoxysilane in a mixture of water and ethanol. The CNT dispersion and sol were mixed at a 5:1 mass ratio, which allowed the colloidal silica to be absorbed onto the outer walls of the tubes. This reaction lasted for 6–8 h and the mixture was continuously agitated in an ultrasonic bath. Subsequently, the SiO_x–CNT were rinsed in ethanol and centrifuged once again. The second step in fabricating SiC–CNT composites involved SPS of SiO_x–CNT. Discs of 15 mm diameter and ≈2 mm thickness were obtained by SPS (SPS-510CE, Fuji Electronic Industrial Co., Ltd.) using a maximum temperature of 1800 °C, heating rate up to 133 °C min^{-1}, holding time of 10 min, and 4 Pa of vacuum atmosphere. SiO_x–CNT powder composition (1 g) was put into the SPS graphite die and pressed at 20 MPa at room temperature. A uniaxial pressure of 80 MPa was applied during the first minute of the heating process (while the temperature was below 600 °C) and maintained during the heating-holding cycle. During the cooling step, the pressure was decreased to 20 MPa.

Micro-Raman spectra and mappings of the produced materials were recorded using a confocal Raman-atomic force microscope (model Alpha300 WITec GmbH) with a 532 nm laser excitation wavelength. Raman maps of 60 × 60 pixels, recording one spectrum per pixel using 0.2 s of acquisition time, were acquired on 10 μm × 10 μm scanned areas. XRD study of the sintered composite was carried out using a PANalytical Empryean X-Ray diffractometer, using a copper $K\alpha$ radiation source. The patterns were collected from different regions on the sample by varying 2θ from 5° to 80°. The microstructure of the sample was observed using a SEM (FEI NanoSEM 630) with a field emission source operated at an acceleration voltage of 5 kV. HRTEM was performed using a JEOL 2010F with an operating voltage of 200 kV, in order to study the interfaces between SiC and CNT within the composite. To generate electron transparent specimens for HRTEM, the standard procedure of cutting, gluing, slicing, grinding, dimpling, and ion milling was performed in sequence on the composite. Ion milling the dimpled sample to electron transparency was carried out by using a low-angle gentle (3 kV) ion beam (Fischione 1010 with a cooling stage) at liquid-nitrogen temperature. EDS analysis of the specimens was also carried out using the same microscope. EFTEM characterization was performed on a JEOL 2010 TEM equipped with a LaB_6 filament, using a 200 kV operating voltage.

Through-thickness thermal diffusivity (α) was measured by the laser-flash method (Thermaflash 2200, Holometrix Netzsch) at room temperature in an Ar atmosphere, using 8.8 × 8.8 mm square specimens with ≈1 mm of thickness. The data reported here correspond to the average of at least three measurements. The thermal conductivity (k) was then calculated using the following expression: $k = \alpha\rho Cp$, where ρ corresponds to the density of the specimen (1.74 g cm^{-3}) and Cp to the specific heat (0.7096 J g^{-1} K^{-1} for graphite).

In order to understand the electronic transport behavior of the SiC–CNT composite, four probe electrical measurements were carried out using a physical property measurement system (PPMS) (Evercool Quantum Design). Thin strips (1.2 × 3 × 1.4 mm) were obtained by cutting the samples with a diamond cutter. The samples were attached to four terminal Cu electrodes with Ag paint. The values of electrical resistance were obtained by passing a current through the material at a constant voltage and the resistivity values were calculated after measuring the dimensions of the sample. The dependence of electrical resistivity on temperature was studied by varying the temperature from 2 to 375 K.

Supporting Information

Supporting Information is available from the Wiley Online Library or from the author.

Acknowledgements

This work was supported by the U.S. Air Force Office of Scientific Research MURI grant FA9550-12-1-0035 and by the Spanish Government under project MAT2012-32944.
Note: Colour in Figure 5 was corrected on August 19, 2015.

Received: April 27, 2015
Revised: June 7, 2015
Published online: July 14, 2015

[1] M. S. Dresselhaus, G. Dresselhaus, P. C. Eklund, A. M. Rao, in *The Physics of Fullerene-Based and Fullerene-Related Materials* (Ed: W. Andreoni), Springer, Netherlands **2000**.
[2] M. Terrones, *Int. Mater. Rev.* **2004**, *49*, 325.
[3] J. M. Romo-Herrera, M. Terrones, H. Terrones, S. Dag, V. Meunier, *Nano Lett.* **2007**, *7*, 570.
[4] G. Lalwani, A. T. Kwaczala, S. Kanakia, S. C. Patel, S. Judex, B. Sitharaman, *Carbon* **2013**, *53*, 90.
[5] A. Peigney, C. Laurent, E. Flahaut, R. R. Bacsa, A. Rousset, *Carbon* **2001**, *39*, 507.
[6] S. Sotiropoulou, N. A. Chaniotakis, *Anal. Bioanal. Chem.* **2003**, *375*, 103.
[7] J. Zhao, A. Buldum, J. Han, J. P. Lu, *Nanotechnology* **2002**, *13*, 195.
[8] D. P. Hashim, N. T. Narayanan, J. M. Romo-Herrera, D. A. Cullen, M. G. Hahm, P. Lezzi, J. R. Suttle, D. Kelkhoff, E. Muñoz-Sandoval, S. Ganguli, A. K. Roy, D. J. Smith, R. Vajtai, B. G. Sumpter, V. Meunier, H. Terrones, M. Terrones, P. M. Ajayan, *Sci. Rep.* **2012**, *2*, 363.
[9] X. Gui, J. Wei, K. Wang, A. Cao, H. Zhu, Y. Jia, Q. Shu, D. Wu, *Adv. Mater.* **2010**, *22*, 617.

[10] J. Zou, J. Liu, A. S. Karakoti, A. Kumar, D. Joung, Q. Li, S. I. Khondaker, S. Seal, L. Zhai, *ACS Nano* **2010**, *4*, 7293.
[11] S. Ozden, T. N. Narayanan, C. S. Tiwary, P. Dong, A. H. C. Hart, R. Vajtai, P. M. Ajayan, *Small* **2014**, *11*, 688.
[12] O. Guillon, J. Gonzalez-Julian, B. Dargatz, T. Kessel, G. Schierning, J. Räthel, M. Herrmann, *Adv. Eng. Mater.* **2014**, *16*, 830.
[13] H. Kwon, M. Estili, K. Takagi, T. Miyazaki, A. Kawasaki, *Carbon* **2009**, *47*, 570.
[14] D.-Y. Kim, Y.-H. Han, J. H. Lee, I.-K. Kang, B.-K. Jang, S. Kim, *Bio. Med Res. Int.* **2014**, *2014*, 768254.
[15] M. Belmonte, J. González-Julián, P. Miranzo, M. I. Osendi, *J. Eur. Ceram. Soc.* **2010**, *30*, 2937.
[16] B. Román-Manso, E. Domingues, F. M. Figueiredo, M. Belmonte, P. Miranzo, *J. Eur. Ceram. Soc.* **2015**, *35*, 2723.
[17] P. Miranzo, C. Ramírez, B. Román-Manso, L. Garzón, H. R. Gutiérrez, M. Terrones, C. Ocal, M. I. Osendi, M. Belmonte. *J. Eur. Ceram. Soc.* **2013**, *33*, 1665.
[18] G. W. Meng, Z. Cui, L. D. Zhang, F. Phillipp, *J. Cryst. Growth* **2000**, *209*, 801.
[19] W.-S. Seo, K. Koumoto, S. Aria, *J. Am. Ceram. Soc.* **2000**, *83*, 2584.
[20] M. Hnatko, D. Galusek, P. Šajgalík, *J. Eur. Ceram. Soc.* **2004**, *24*, 189.
[21] V. D. Krstic, *J. Am. Ceram. Soc.* **1992**, *75*, 170.
[22] A. W. Weimer, K. J. Nilsen, G. A. Cochran, R. P. Roach, *AIChE J.* **1993**, *39*, 493.
[23] E. T. Thostenson, P. G. Karandikar, T.-W. Chou, *J. Phys. Appl. Phys.* **2005**, *38*, 3962.
[24] R. Z. Ma, J. Wu, B. Q. Wei, J. Liang, D. H. Wu, *J. Mater. Sci.* **1998**, *33*, 5243.
[25] S. Yajima, K. Okamura, T. Matsuzawa, Y. Hasegawa, T. Shishido, *Nature* **1979**, *279*, 706.
[26] Y.-J. Lee, *Diamond Relat. Mater.* **2004**, *13*, 383.
[27] Q. Huang, D. Jiang, I. A. Ovid'ko, A. Mukherjee, *Scr. Mater.* **2010**, *63*, 1181.
[28] T. F. Lam, R. Sharma, J. Liddle, J. P. Winterstein, P. Kabro, *Microsc. Microanal.* **2012**, *18*, 1530.
[29] E. García, M. I. Osendi, P. Miranzo, *J. Appl. Phys.* **2002**, *92*, 2346.
[30] E. García, R. Barea, M. I. Osendi, P. Miranzo, *Key Eng. Mater.* **2004**, *264*, 2179.
[31] P. Miranzo, E. García, C. Ramírez, J. González-Julián, M. Belmonte, M. I. Osendi, *J. Eur. Ceram. Soc.* **2012**, *32*, 1847.
[32] K. Yang, J. He, P. Puneet, Z. Su, M. J. Skove, J. Gaillard, T. M. Tritt, A. M. Rao, *J. Phys. Condens. Matter* **2010**, *22*, 334215.
[33] G. L. Harris, *Properties of Silicon Carbide*, INSPEC, London **1995**.
[34] J. Sánchez-González, A. L. Ortiz, F. Guiberteau, C. Pascual, *J. Eur. Ceram. Soc.* **2007**, *27*, 3935.
[35] G. Sauti, A. Can, D. S. McLachlan, M. Herrmann, *J. Am. Ceram. Soc.* **2007**, *90*, 2446.
[36] K. Yang, J. He, Z. Su, J. B. Reppert, M. J. Skove, T. M. Tritt, A. M. Rao, *Carbon* **2010**, *48*, 756.
[37] S. I. Cha, K. T. Kim, K. H. Lee, C. B. Mo, Y. J. Jeong, S. H. Hong, *Carbon* **2008**, *46*, 482.
[38] T. W. Ebbesen, H. J. Lezec, H. Hiura, J. W. Bennett, H. F. Ghaemi, T. Thio, *Nature* **1996**, *382*, 54.
[39] N. F. Mott, *Philos. Mag.* **1969**, *19*, 835.
[40] H. M. Kim, M.-S. Choi, J. Joo, S. J. Cho, H. S. Yoon, *Phys. Rev. B* **2006**, *74*, 054202.
[41] M. Pinault, M. Mayne-L'Hermite, C. Reynaud, O. Beyssac, J. N. Rouzaud, C. Clinard, *Diam. Relat. Mater.* **2004**, *13*, 1266.
[42] T. Seeger, Ph. Redlich, N. Grobert, M. Terrones, D. R. M. Walton, H. W. Kroto, M. Rühle, *Chem. Phys. Lett.* **2001**, *339*, 41.